Volume 16
Number 34
14 September 2025
Pages 15283–15744

Chemical Science

rsc.li/chemical-science

ISSN 2041-6539

ROYAL SOCIETY OF CHEMISTRY

EDGE ARTICLE
Chris Ritchie *et al.*
Planarisation or a twist? Using steric engineering to unlock the origin of mechanofluorochromic red-shifts

15 YEARS ANNIVERSARY

Chemical Science

ROYAL SOCIETY OF CHEMISTRY

EDGE ARTICLE

View Article Online
View Journal | View Issue

Cite this: *Chem. Sci.*, 2025, **16**, 15320

All publication charges for this article have been paid for by the Royal Society of Chemistry

Received 11th June 2025
Accepted 18th July 2025

DOI: 10.1039/d5sc04257g

rsc.li/chemical-science

Planarisation or a twist? Using steric engineering to unlock the origin of mechanofluorochromic red-shifts†

Peter W. McDonald, [a] Lars Goerigk [b] and Chris Ritchie *[a]

Engineering the ground-state orientations of donor and acceptor groups through steric control of fluorophore conformations is an effective strategy for manipulating molecular electronics and, in turn, their emissive properties. Where strong emission is retained in the crystalline state, a correlation of structure with photophysical properties can be made, as is the case for the five pyridinium betaines reported herein. Our findings provide strong evidence that an increase in dihedral angle between *N*,*N*-diphenylamino donor and pyridinium acceptor induces a notable red-shift in emission maximum, with the mechanofluorochromic response also correlated with the same process. This research aims to address the oft-invoked explanation that planarisation induces red-shifted emission, highlighting that this effect is not universal and that systematic studies are essential. Further, this elegant steric engineering approach may be applied to other mechanochromic systems to determine the nature of their geometry changes.

Introduction

Elucidating the reason why a compound exhibits a change in emission profile on application of mechanical force is not trivial and is an important aspect to consider when attempting to design new classes of such compounds or applying them in functional materials.[1] When considering fluorescence, this phenomenon is known as mechanofluorochromism (MFC) and there are some well-established design principles to help induce it, such as imbuing molecules with charge transfer character and sterically bulky groups to prevent aggregation-caused quenching.[2,3] Intramolecular charge transfer (ICT) requires a molecule containing at least one electron donor and one electron acceptor. When such a molecule is excited, a change in dihedral angle can result in the molecule moving along its potential energy surface, leading to relaxation to a local energy minimum, known as a twisted intramolecular charge transfer (TICT) state.[4] This increase in dihedral angle (usually to ~90°) occurs about a bond that connects the donor and acceptor and results in a red-shifted and quenched emission, compared to the initial state. The increase in dihedral angle between donor and acceptor also leads to a greater degree of spatial separation between frontier orbitals and thus a greater degree of charge transfer when a transition occurs.[5] Intuitively, a TICT state would be classified as less planar than the initial conformation. Contrastingly, it is well evidenced that an increase in π-conjugation leads to a spectral red-shift (be it absorption or emission) and that this is the result of a more planar conformation yielding a higher degree of p-orbital overlap. While this may apply generally to conjugated π-systems without charge separation, it may also occur as a relaxation mechanism in donor–acceptor systems, where it is known under various terminology, depending on the precise nature of the geometry change.[6,7] Thus, an emission red-shift can potentially be achieved by two opposing geometry changes, towards a larger or smaller dihedral angle between a donor and an acceptor, relative to the ground state. It is important to note that these are not the only proposed geometrical changes that can lead to red-shifts (*e.g.* rehybridisation, bond-length changes, *etc.*).[8] Herein lies the crux of the issue, namely, how can the direction or type of the geometry change be elucidated? This raises further questions, such as how do we define a net change in planarity when there is more than one rotatable aromatic ring?[9] And can it be different in solution compared to the solid-state? Theoretical calculations provide valuable insight, but these need to be rigorously backed up by experimental evidence, which is not always conclusive, and calculation outputs are dependent on the level of theory chosen.[10,11] Two prime examples highlighting the relevance of this issue (specifically for solution-state studies) are 4-(*N*,*N*-dimethylamino)benzonitrile (DMABN) and nile red, fluorophores whose proposed excited-state relaxation mechanisms include planar-ICT (PICT) and TICT.[8] Both have been studied for decades and the nature of their relaxation

[a]*School of Chemistry, Monash University, Wellington Road, 3800, Australia. E-mail: Chris.Ritchie@monash.edu*

[b]*School of Chemistry, The University of Melbourne, 3010, Australia*

† Electronic supplementary information (ESI) available. CCDC 2457183–2457196. For ESI and crystallographic data in CIF or other electronic format see DOI: https://doi.org/10.1039/d5sc04257g

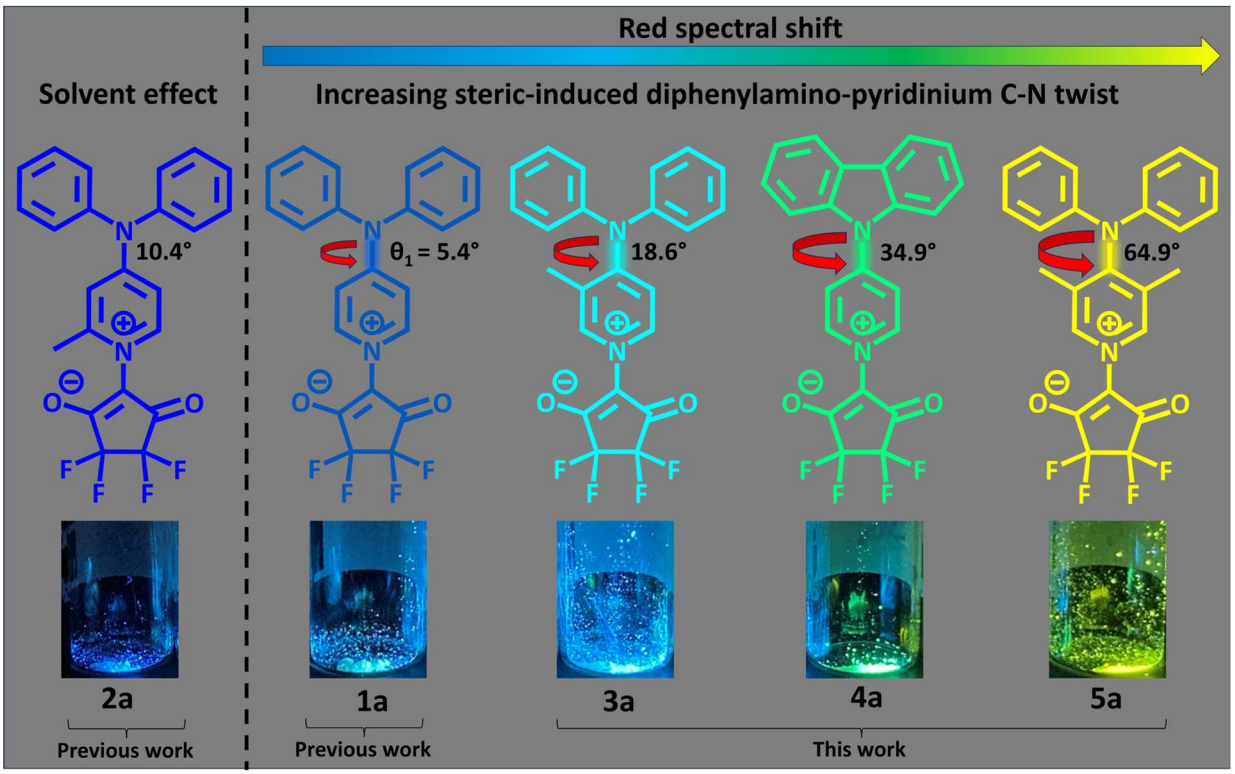

Fig. 1 Graphical explanation of the hypothesised rationale for red-shifting emission, including the structures of the main compounds under study, their average *N*,*N*-diphenylamino-pyridinium C–N dihedral angles (θ_1), as well as representative images of their crystalline emissions under 365 nm irradiation. Emission images are a qualitative guide. For **1a**, **3a**, **4a**, and **5a**, an increase in the *N*,*N*-diphenylamino-pyridinium C–N dihedral angle leads to overall average, red-shifted fluorescence maxima. For **2a**, solvent inclusion in the crystal structure complicates the analysis, hence it is not directly comparable.

mechanisms are still hotly debated to this day.[12] To add to the complexity, the definitions of PICT and TICT do not encompass all possibilities, such as 90° planarisations or smaller magnitude increases in dihedral angles.[13] Planarised intramolecular charge transfer (PLICT) specifically refers to a ground state where a donor and acceptor are perpendicular.[6] Planarisation about a single bond connecting them (*via* an intermediate donor) occurs in the excited state. This is essentially the opposite to TICT. PICT differs in that the initial geometry is planar and rehybridisation from pyramidal to planar sp^2 nitrogen or formation of a quinoidal form occurs in the excited state.

To further illustrate the issue, many reports of mechanofluorochromism attribute the red-shift observed after mechanical force to planarisation of the conjugated π-systems,[14] sometimes when concurrently invoking TICT states in solution.[15] This is particularly evident in triphenylamine (TPA) derivatives, which are structurally similar to the compounds presented herein.[16] It is suggested here that for a given compound, if the solution-state emission shows the same spectral shift trend with increasing polarity as it does in the solid-state on application of force, it is unlikely that opposing mechanisms occur in solution and solid-states (*i.e.* if the direction of the spectral shift with increasing polarity is the same as that after applying force, and either PLICT or TICT is assigned as the mechanism in solution, then it should be the same mechanism in the solid-state).[17] Unless, of course, detailed evidence is provided for both cases, such as an excited state potential energy surface indicating multiple energetically-accessible conformations.[18] Importantly, this example assumes no mechanisms other than geometry changes are involved. We are not the first to notice and address this issue in the literature, however, the confusion persists.[19] In an attempt to provide clarity and ascertain the nature of the geometry change, a simple methyl group substitution is utilised to test whether increasing the dihedral angle (decreasing planarity) between either a *N*,*N*-diphenylamino or enolate donor, and pyridinium acceptor induces a red or blue-shift in emission. This methylation approach has been utilised successfully before to study solution state emission in relation to TICT and PICT states, as well as tuning singlet-triplet state energy gaps, however, to the best of our knowledge, it has not been applied in relation to solid-state emission to solve the nature of the geometry change in MFC compounds.[20–22] Thus, we decided to test the methyl "pre-twisting" strategy on a novel set of pyridinium betaines (PBs), building on our previously studied compounds by introducing three new PBs (**3a–5a**) with varying dihedral angles and degrees of planarity/rigidity (Fig. 1).

This approach provides convincing evidence that allows one to answer the question of the nature of the geometry change. Namely, increasing the dihedral angle between the *N*,*N*-

diphenylamino and pyridinium acceptor red-shifts the emission, agreeing with a TICT-like excited state. In this context, a TICT state refers to a 90° dihedral angle between donor and acceptor in the relaxed excited state, whereas TICT-like requires an increase in dihedral angle in the relaxed excited state, but not necessarily to 90°. This mechanistic explanation arises from the donor–acceptor–donor′ (D–A–D′) electronic structure of these molecules and is graphically illustrated in Fig. 1, however, this type of electronic structure is far less-common than simpler donor–acceptor molecules that are ubiquitous. The additional donor adds a layer of complexity to the initial question on the nature of the geometry change we set out to answer, however, our systematic approach has identified the orientation of the *N*,*N*-diphenylamine donor with respect to the remainder of the molecule as critically responsible for the red-shifted emission in solution and the mechanically ground solid-state. We have previously shown this in a pure D–A analogue that used boron trifluoride to create the pyridinium acceptor.[23] In this way, the complication of a second donor was avoided. Here, we primarily focus on sterically tuning the *N*,*N*-diphenylamino-pyridinium dihedral angle to show that increased dihedral angle, and not planarisation, is responsible for the MFC red-shift. A key advantage of applying this approach to the solid-state is the ability for direct comparison between structure and emission properties. This approach may prove to be fruitful for ascertaining the nature of the geometry changes in various other MFC systems.

Results and discussion

Synthesis and optical properties

Scheme 1 shows the synthetic pathways to the newly prepared compounds for this study. Firstly, 3,5-dimethylpyridine (3,5-lutidine) was reacted with octafluorocyclopentene in THF, with addition of a small amount of water, to form the lutidine betaine (**Lut-bet**) with a 37% yield, as per our previously published procedure.[24] This was prepared as a control to account for potential methyl inductive electronic effects. Next, three pyridyl precursors (**3**–**5**) were synthesised using copper-catalysed Ullmann-type coupling,[25] with **4** being prepared following an alternative literature procedure.[26] Yields for **3** and **5** were low (34 and 14%, respectively), presumably due to addition of the methyl groups in the 3 and/or 5 positions of pyridine giving rise to steric hindrance, along with reduced reactivity of secondary amines under these conditions resulting in a mixture of monosubstituted and disubstituted products. Conversely, the carbazole precursor requires formation of only one C–N bond and thus **4** was prepared with a good yield of 81%. Finally, the corresponding PBs (**3a**–**5a**) were synthesised in moderate to high yields (49, 33 and 94%, respectively) by addition of octafluorocyclopentene to the relevant precursor, following the same procedure as **Lut-bet**. All new compounds were extensively characterised using standard techniques (see ESI S1 – Experimental section for details†). Attempts to synthesise the 2,6-dimethyl-*N*,*N*-diphenylaminopyridine analogue were unsuccessful, most likely due to the additional steric hindrance preventing nucleophilic attack by the pyridine lone pair. Rather,

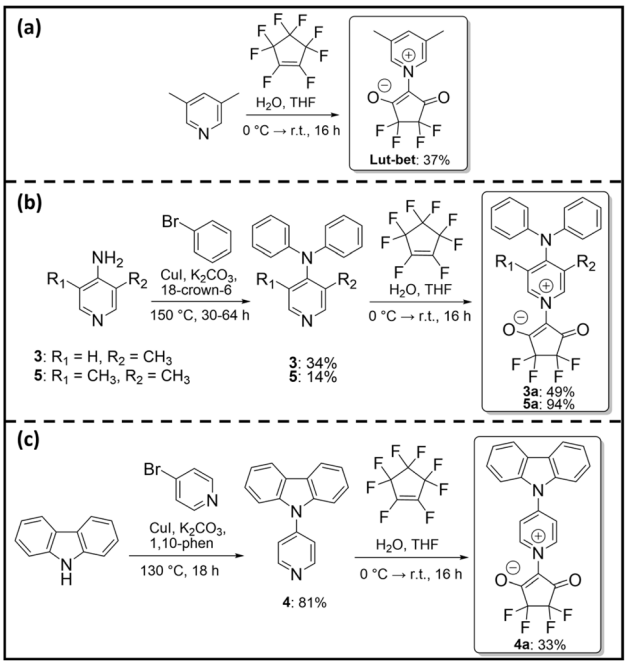

Scheme 1 Synthetic pathway to (a) lutidine betaine (**Lut-bet**); (b) precursors (**3** and **5**) and corresponding betaines (**3a** and **5a**); (c) carbazole precursor (**4**) and corresponding betaine (**4a**).

the product isolated from this reaction is an ionic compound ($C_{24}H_{19}F_5N_2O_2$ – **6H$^+$ enolate**), which was characterised crystallographically, and its structure is reported herein, along with that of its precursor (**6**).

Before detailing the PBs, an important assumption in this research will be considered. It is assumed that the additional methyl groups do not red-shift the emission, which would result in a confounding variable. This methylation approach is well-established and assumes that these groups are electronically innocent.[27] Nevertheless, to address the impact of the methyl groups on the solid-state emission spectra, **Lut-bet** is compared to the previously reported unmethylated pyridine betaine (**Pyr-bet**).[24] An important caveat is that both compounds contain partially occupied solvent, which is assigned as a water molecule in the unit cell and this may affect the emission through mechanisms including interaction-induced conformation differences or intermolecular energy transfer. Therefore, steady-state emission measurements were performed on dry material (150 °C for 1 hour, the temperature above which TGA shows no discernible water content), as well as undried crystalline material. The fluorescence maxima for dried **Pyr-bet** and **Lut-bet** are 420 nm and 414 nm, respectively, indicating a subtle blue-shift in the methylated analogue (Fig. 2). A comparison of the dried and undried samples is given in Fig. S1,† showing that the solvent broadens and slightly red-shifts the emission spectra, most noticeably in **Pyr-bet** (λ_{max} 428 nm), where the solvent occupancy is higher, as determined from crystallographic, TGA and FTIR data. **Pyr-bet** contains a partial water molecule above the enolate carbonyl groups, which is consistent with a weak n → π* interaction. The O···C distance is 3.18 Å, which is slightly

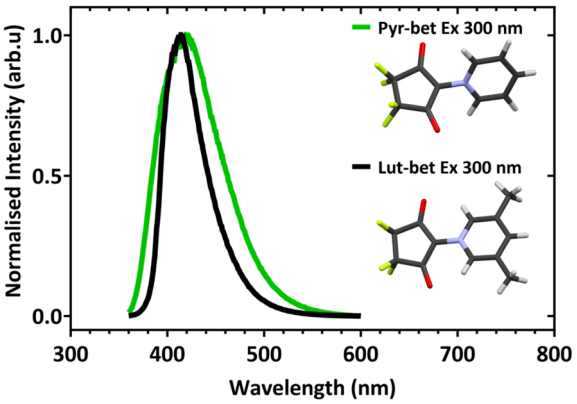

Fig. 2 Solid-state crystalline fluorescence spectra of dried **Pyr-bet** (λ_{max} 420 nm) and **Lut-bet** (λ_{max} 414 nm). Inset: excitation wavelengths and depictions of their structures determined by SC-XRD. Spectra are cut above double the excitation wavelength.

less than the sum of the van der Waals radii (3.22 Å) and the O···C═O angle is 101.6°, which falls approximately along the Bürgi-Dunitz trajectory for such an interaction.[28] In **Lut-bet** this interaction is replaced by a similar enolate oxygen to carbonyl interaction. Delayed emission was also detected with maxima of ~420/520 nm in **Pyr-bet** (Fig. S1c†) and ~414/520 nm in **Lut-bet** (Fig. S1f†), with the broad lower energy peak contributing significantly for **Pyr-bet** at 0.1 ms delay time but the corresponding lower energy peak in **Lut-bet** only becoming more prominent at a longer delay time of 1 ms (Fig. S1f†). It is noteworthy that methyl groups have been shown to induce blue-shifts in phosphorescence in the gas phase but that is not apparent here.[29] In this case, the delayed spectra partially overlay with the prompt emission spectra, indicating some long-lived decay from the singlet state, as well as a weaker intensity lower energy phosphorescence band. This was qualitatively observed as a green after-glow in both compounds on cooling the samples to ~77 K. While this data suggests that the methyl groups are not entirely electronically innocent, they minimally perturb the emission maxima and thus methyl group substitution is a valid approach to study the geometry effect. This is important as the methyl groups can be ruled out as inducing red-shifts.

The three new PBs (**3a–5a**) were hypothesised to exhibit red-shifting emission profiles with increasing steric-induced twisting about the *N*,*N*-diphenylamino-pyridinium C–N bond (θ_1 – Fig. 1). The rationale for designing these PBs was that the same mechanism proposed for the MFC red-shifts in previously published **1a** and **2a** will still hold and can be tested.[30] That is, when the dihedral angle increases (from 0° up to a maximum of ~90°) between the *N*,*N*-diphenylamino and pyridinium moieties, the emission will gradually red-shift (TICT-like). They should also show MFC with red-shifts on application of anisotropic mechanical force, just like **1a** and **2a**, due to larger dihedral angles being attainable in amorphous forms. Furthermore, if an MFC red-shift is observed, a planarisation mechanism can be ruled out, due to steric hindrance blocking planarisation about this bond.

The pyridyl precursors **3–5** exhibit fluorescence in crystalline form, as well as delayed emission components at lower energies, attributed to phosphorescence (Fig. S2 and Table S1†). The solid-state fluorescence of **4** has previously been reported.[31] The longer wavelength emission bands present in the steady-state spectra (most prominent in **5**) are assigned as phosphorescence, which is supported again qualitatively by after-glows on cooling the samples to ~77 K. Of note is the considerable overlap between fluorescence emission and phosphorescence excitation spectra in **3** and **4**, which can result in reabsorption and enhanced excited-state population.

Formation of the corresponding PBs (**3a–5a**) enhances the ICT character by converting pyridine to the electron deficient pyridinium moiety and red-shifting the absorption and emission profiles. Solution-state spectra reveal subtle negative solvatochromism (absorption) and strong positive solvatofluorochromism (emission) for all three PBs. The lowest energy absorption bands are reported and assigned as CT states, and the emission bands are also assigned as CT states (Fig. S3–S5†). The opposing types of absorption and emission chromism lead to increasing Stokes shifts with increasing solvent polarity. Fluorescence lifetimes and quantum yields decrease with increasing polarity as expected for ICT states (Tables S2–S4†). The decrease in fluorescence quantum yield is consistent with a forbidden TICT state emission, as well as the energy gap law.[32] While **3a** and **5a** are very similar, the emission maxima are slightly blue-shifted in **4a**. The similarity in emission maxima and peak shape for all three PBs is important. The strong similarity suggests emission from similar excited states, regardless of the ground-state geometry. In this case it is attributed to a TICT-like state, as **3a** and **5a** cannot planarise about the *N*,*N*-diphenylamino-pyridinium C–N bond due to the blocking methyl groups, and **4a** likely cannot planarise due to intramolecular hydrogen–hydrogen contacts presenting an energetic barrier to planarisation. There is some subtle vibronic structure in the lowest lying CT absorption band of **4a** in less polar solvents (toluene and dichloromethane – Fig. S4†). This is attributed to the planar carbazole moiety providing enhanced rigidity. To summarise the solution data, all three PBs are reaching a similar, twisted excited-state geometry in the relatively conformationally-unrestrictive solution state. This is not expected to be the case in the conformationally-restrictive crystalline forms.

To gain a better understanding of the solid-state emission properties, the spectra of the two previously published PBs, **1a** and **2a**, are included, in addition to the three new PBs.[30] A comparison of all five PBs in four physical forms is provided in Fig. 3. The forms were chosen to match previous data on **1a** and **2a**, giving information on the solvent-induced and thermal reversibility: C = crystalline powder, G = mechanically ground sample (mortar and pestle, ~10 min), R = mechanically ground sample exposed to solvent to facilitate reordering, An = R samples annealed for 1 hour at 100 °C. The excitation spectra in Fig. 3a reveal a gradual red-shifting of the lowest energy maximum peak in the order **2a**, **1a**, **3a**, **4a**, **5a**. A grey reference bar is marked at 376 nm indicating the maximum of **1a**-C. Comparison of **1a** and **3a** shows that the two main broad bands

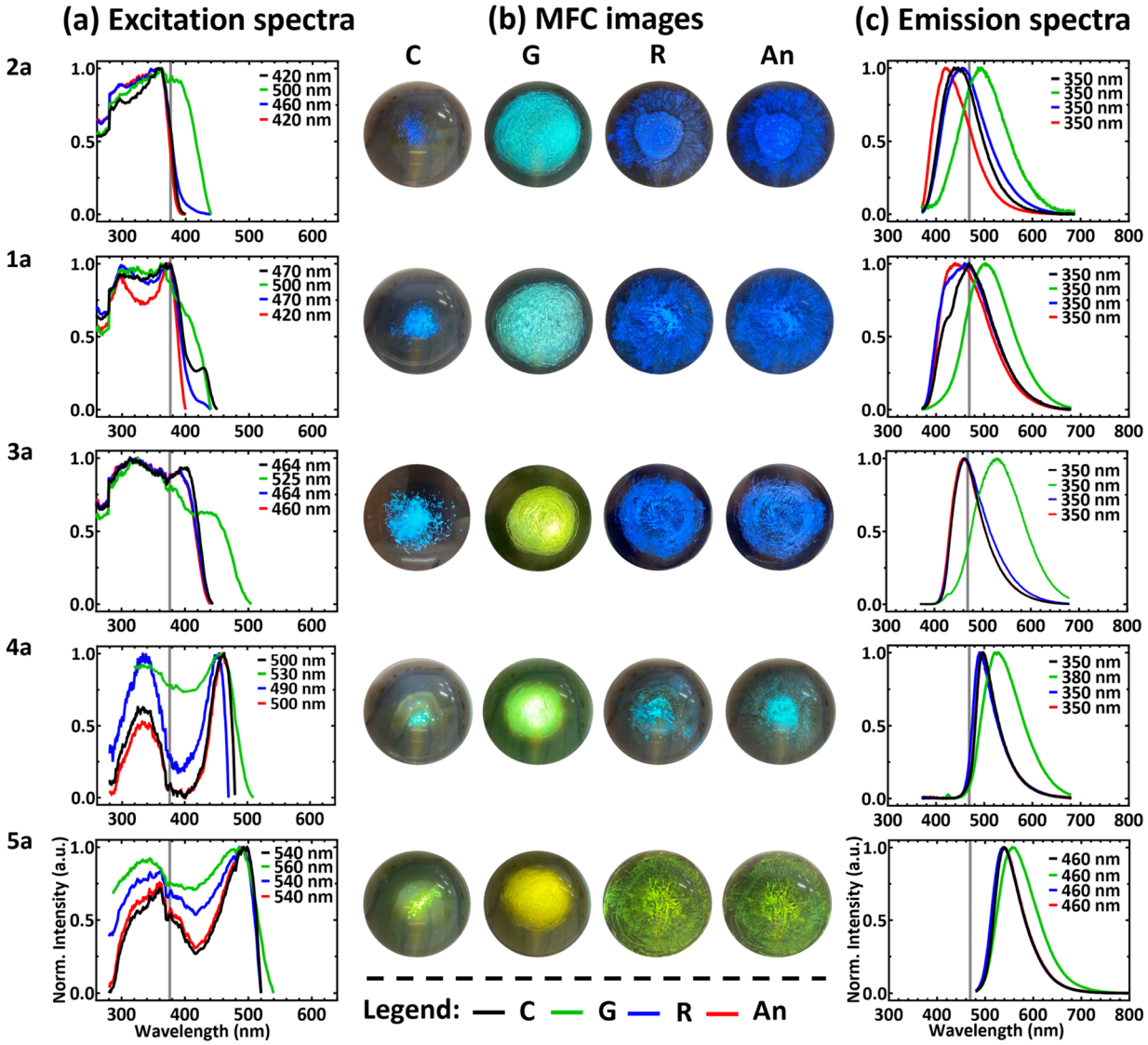

Fig. 3 MFC behaviour of the five PBs under study. From top to bottom: **2a**, **1a**, **3a**, **4a** and **5a**. (a) Excitation spectra with a grey solid vertical bar at 376 nm indicating the excitation maximum of **1a**-C as a reference point. The detection wavelength is indicated in each graph legend and spectra were cut below half the detection wavelength; (b) representative MFC images of the four physical forms under UV irradiation at 365 nm (images are included as a qualitative guide and not the actual samples used for measurements); (c) emission spectra for the four forms with a grey solid vertical bar at 469 nm indicating the emission maximum of **1a**-C as a reference point. Excitation wavelengths are given in the legend, and spectra were cut above twice the excitation wavelength. Excitation and emission spectra and images of **1a** and **2a** are reproduced from previously published research with permission and are copyright RSC (*J. Mat. C*).[3]

are red-shifted in **3a** and that the lower energy band in **3a**-G is more prominent than in **1a**-G. In **4a** and **5a**, both of these broad bands are even further red-shifted, and a key feature is that there is far less change after force application (relative to the C, R and An forms). The lower energy band in **4a**-G and **5a**-G is broader than in the other forms and a subtle blue-shift is detected in both bands of the excitation spectrum in **5a**-G (relative to the C, R and An forms). Fig. 3b provides representative visual images of all five PBs in the four forms under 365 nm irradiation. The corresponding emission spectra are given in Fig. 3c, again with a reference bar at 469 nm representing the emission maximum for **1a**-C. As predicted, a red-shift in emission maximum occurs from **3a**-C to **4a**-C to **5a**-C, with maxima of 462, 496 and 540 nm, respectively (Table 1). **2a**-C represents the most blue-shifted maximum at 437 nm and the blue-shift relative to **1a** may be caused by several factors. These include the fact that **2a** crystallises with solvent inclusion, electronic effect of the additional methyl group, and a lower number of available conformational states due to the methyl group suppressing rotation. The first factor can result in specific interactions that alter the emission profile, the second factor was seen as having a minor influence in **Lut-bet**, and the third factor may result in a sharper emission band and apparent blue-shift due to less emissive states. The similar band onsets for **1a** and **2a** support this notion. Due to these complications, it is difficult to compare **2a** with the other PBs, thus the main

Table 1 Solid-state fluorescence properties of **3a**, **4a** and **5a**

	Form	λ_{max} nm	$\tau_1{}^a$ (%) ns	$\tau_2{}^a$ (%) ns	$\tau_{avg}{}^b$ ns	χ^2
3a	C	462	3.08(52)	6.12(48)	4.54	1.054
	G	529	3.30(19)	8.14(81)	7.22	1.060
	R	462	3.22(46)	7.33(54)	5.44	1.098
	An	459	2.96(56)	6.07(44)	4.34	1.098
4a	C	496	2.79(50)	6.13(50)	4.46	1.102
	G	524	2.64(33)	7.54(67)	5.90	1.097
	R	490	2.87(58)	6.63(42)	4.45	1.045
	An	496	2.53(87)	6.14(13)	2.99	1.000
5a	C	540	4.18(14)	9.88(86)	9.09	1.029
	G	558	2.94(24)	8.64(76)	7.30	1.134
	R	538	3.79(19)	8.77(81)	7.85	1.117
	An	540	5.07(12)	10.22(88)	9.61	1.016

[a] Fractional intensities. [b] Intensity weighted average lifetime.

comparison is between the other four PBs, all of which crystallise without inclusion of solvent in the lattice. After force application, **3a** exhibits the largest MFC red-shift (Δ67 nm), followed by **4a** (Δ28 nm), and finally **5a** shows the smallest MFC shift (Δ18 nm). After solvent exposure, blue-shifts were observed in all three compounds to give spectra that closely resemble the respective C forms. After annealing the R forms, a slight blue-shift was measured in **3a** and slight red-shifts in **4a** and **5a**. Full width at half maximum (FWHM) values for **4a**-C (1958 cm^{-1}) and **5a**-C (2190 cm^{-1}) are significantly smaller than that of **3a**-C (3980 cm^{-1}), which indicate a greater colour purity for the former two PBs. For **3a–5a**, the C, R and An forms resemble one another more closely than **1a** and **2a**, indicating less available conformational states due to the steric restrictions. A consequence of large geometry changes on excitation is access to additional vibrational and conformational relaxation pathways, resulting in broadened emission bands, and this helps to explain why the FWHM for **4a**-C and **5a**-C are smaller than **3a**-C (as well as the broader spectra of **1a** and **2a**).[33] The fluorescence decays were fit with two exponentials in all cases with satisfactory χ^2 values (Table 1). **3a** and **4a** behave similarly, with a dominant contribution from the shorter component in the C form, then an increasing contribution from the longer lifetime component in the G form, followed by an increasing shorter contribution on reordering and annealing, aligning with the cyclability between solid states. Notably, **5a** behaves differently, with the longer component dominant in all four forms. Both components become shorter in the G form, with an increased proportion of the shorter component. Due to the sterically bulky geometries of the PBs and lack of close π···π interactions it is unlikely that excimer formation is possible, however other intermolecular energy transfer pathways are plausible. An alternative explanation for two decay components is a mixture of LE and CT states, or even two CT states, considering the two donors. The contribution of each state to the transition depends on the angle between donor and acceptor, with more CT character generally observed when the angle increases.[34] Thus, increasing the angle towards 90° may increase the percentage of the CT state and lower the contribution of the LE state, or shift the balance between two CT states. The behaviour seen in **5a** may stem from a decrease in the magnitude of the lifetime above a certain dihedral angle only achieved in **5a**-G. However, the data on **5a** suggests that it may not be as simple as just a mixture of LE and CT states. The fluorescence maxima and lifetimes for **3a–5a** are summarised in Table 1. Like the precursors, the presence of delayed emission was detected in each PB (Fig. S6†), with a remarkable decrease in the singlet-triplet energy gap to close to zero in **4a**-C and **5a**-C, relative to **3a**-C, as inferred from band onsets, and the prompt and delayed emission maxima (Table S5†). This emission is attributed to room temperature phosphorescence (RTP) in **3a**, with a probable mixture of thermally-activated delayed fluorescence (TADF) and RTP in **4a**-C, and exclusive TADF occurring in **5a**-C, due to the near identical overlay of the prompt and delayed spectra.[22] However, it is important to state that microsecond and millisecond decays are required to unequivocally assign these processes, but that is beyond the scope of this study. One of the requirements for effective TADF is a small singlet-triplet energy gap to facilitate reverse intersystem crossing, and this has been shown to be dependent on the geometry between donor and acceptor, with a more twisted orientation lowering the gap, while also reducing the frontier orbital energy gap.[5,34,35] RTP and TADF are highly sought after phenomena in organic materials and both have utility in various optical applications.[36] Overall, the solid-state emission maxima red-shift from **3a** to **4a** to **5a** and the MFC red-shift decreases in the same order. To rationalise these properties structural analysis is instructive.

Structural analysis

Crystallography is an invaluable tool to help discern structure–property relationships. The crystal structures of **6**, **6H$^+$ enolate**, **Lut-bet**, and the three precursors (**3**, **4**, and **5**) were collected at 123 K and are reported with key interactions shown in Fig. S7 and S8† (crystallographic details in Tables S6 and S7†). No π···π interactions were observed in **3** or **5**, instead the key interactions are CH···π (3.40 Å) and CH···N (2.48 Å), respectively. Precursor **4** has previously been reported, and was crystallised with the same unit cell parameters and chiral space group $P2_12_12_1$, exhibiting π···π interactions between carbazole rings (~3.4 Å).[37] These observations were expected due to the twisted conformations accessible through the phenyl rings, indicating that only **4** or corresponding PB **4a** might show intermolecular energy transfer *via* π···π interactions. For the precursors, when including the previously reported **1** and **2**, a linear correlation is observed between the average dihedral angle about the *N*,*N*-diphenylamino-to-pyridine C–N bond (θ_1) and its corresponding bond length (C_P–N_1) (Table S8 and Fig. S9†). Notable elongation of this bond occurs as the dihedral angle increases, indicating electronic decoupling.

Crystal structures for the PBs were collected at 123 K and room temperature to better represent the conditions of the emission experiments and check for any temperature-induced phase changes (crystallographic details in Tables S9–S11†). No phase changes were observed, only the expected thermal expansion at elevated temperature. The room temperature

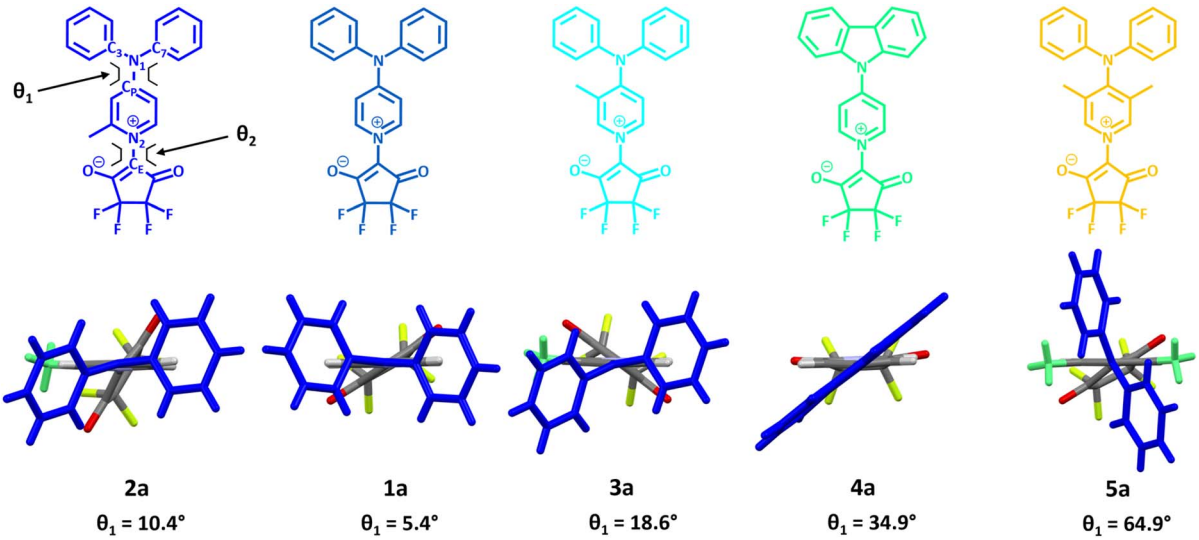

Fig. 4 The molecular structures of **1a**–**5a**, with labelling of key atoms and dihedral angles given on **2a** (left) that apply to all five PBs. θ_1 is the dihedral angle that primarily red-shifts the emission. Below are the corresponding room temperature crystal structures looking down the *N*,*N*-diphenylamino-pyridinium C–N bond, with the *N*,*N*-diphenylamino moiety in blue and methyl groups in green. The structure of **4a** shows only one of the three representative molecules in the asymmetric unit, which each have different geometries. θ_1 is the average of the three molecules.

structures will be exclusively discussed hereafter. The complication of solvent effects is avoided here as none of the PBs incorporated solvent in their crystal structures. All three PBs exhibit intra and/or intermolecular CH···O interactions (Fig. S10†). Hirshfeld surface analysis (CrystalExplorer) shows that these are some of the closest interactions and account for 13.7, 13.3 and 13.7% of the surface area in **3a**, **4a**, and **5a**, respectively (Fig. S11†). **3a** was crystallised in the same space group as **1a**, with very similar unit cell parameters and packing, and these will be discussed and compared in the next section. Three molecules with subtly different geometries make up the asymmetric unit of **4a**. There are three types of π···π interactions in **4a**, two between carbazole–carbazole moieties with centroid–centroid distances of 3.62 and 3.71 Å, and one between carbazole-pyridinium moieties at 3.78 Å. However, these are longer than those found in **4** and greater than two times the van der Waals radius of carbon (3.4 Å), thus likely weak. A notable CF···N interaction is seen in **5a** (2.80 Å, 151°, sum of *F*/*N* van der Waals radii = 3.02 Å).[38] This short interaction is known to occur between fluorine and pyridinium moieties.[39] One possible outcome of this CF···N interaction is a contribution to the elongation of both lifetime components measured in the C, G and An forms of **5a**. Another important aspect of fluorine is that it has been shown to enhance photoluminescence efficiency in condensed states relative to non-fluorinated analogues, due to intermolecular H···F interactions suppressing molecular motion.[40] All three PBs show significant CH···F interactions, accounting for 26.5, 31.3 and 23.7% of the Hirshfeld surface area in **3a**, **4a** and **5a**, respectively, and which likely contribute to suppressing non-radiative relaxation pathways.

Several key structural parameters will be discussed next, the *N*,*N*-diphenylamino-pyridinium and enolate-pyridinium C–N bond lengths (C_P–N_1 and C_E–N_2, respectively) and corresponding *N*,*N*-diphenylamino-pyridinium and enolate-pyridinium average dihedral angles (θ_1 and θ_2, respectively), as well as the pyramidal nature of N_1 (φ), and the quinoidality factor of pyridinium (Q_f). Increasing the average dihedral angle between the *N*,*N*-diphenylamino moiety and the pyridinium ring (θ_1) correlates with an average red-shift in emission in the order **1a** (5.4°), **3a** (18.6°), **4a** (34.9°), **5a** (64.9°). This change in dihedral angle is not symmetrical for each phenyl ring in a given PB and this can be seen by looking down C_P–N_1 (Fig. 4). Of note, θ_1 spans from 29.2 to 39.5° in the three conformations of **4a**, a range of 10.3°. With a θ_1 of 10.4°, **2a** does not fit into this trend, but due to it crystallising with various solvents incorporated, it has the potential for specific interactions and is thus not comparable. There is significant variation in θ_2, with **2a** showing the largest value of 58.0° due to the steric effect of the methyl group (Table S12†). **1a**, **3a**, and **5a** have similar values of 32.0, 36.2, and 31.4°, respectively, while θ_2 spans from 2.7 to 42.2° (a range of 39.5°) in the three conformations of **4a**, which is greater than three times the range of its θ_1 variation. Recall that **4a** has the sharpest emission band. This suggests that θ_2 is not the dominant factor in the emission variation between these three PBs. The bond length C_E–N_2 remains mostly unchanged across all five PBs, ranging between 1.424 and 1.433 Å. C_P–N_1 contracts going from precursor to PB indicating enhanced donation of electron density from the amine nitrogen lone pair into the electron deficient pyridinium moiety. Like the precursors, C_P–N_1 shows a linear correlation with θ_1 ranging from 1.351 to 1.415 Å (Fig. S12†). This is to be expected, as the amine nitrogen lone pair will be less available for electron donation with increasing dihedral angle. This results in an increasing degree of electronic decoupling with increasing dihedral angle and is consistent with TICT theory.[20] Pyramidalisation of nitrogen is a proposed

factor in red-shifting emission, so this was measured for N_1 as the angle (φ) between the plane formed by N_1 and the two bonded carbons in each phenyl ring ($C_3N_1C_7$) and the vector C_P–N_1 (see Fig. 4 for labelling schematic).[20] For all the PBs, φ is between 0 and 2.7°, indicating a low degree of pyramidalisation (Table S13†). This shows that there is no correlation between θ_1 and φ in the ground state geometry but does not rule out φ increasing in the excited state. The quinoidal nature of the pyridinium moiety is another factor that can influence the emission and is measured as the ratio of two bonds in the pyridinium ring known as Q_f.[20] A larger value of Q_f indicates less quinoidal nature. For the PBs there is a general trend of decreasing quinoidal nature as C_P–N_1 increases (Table S13†). This indicates that increasing the quinoidal nature correlates with blue-shifted emission, which means the red-shifted emission cannot be explained by a quinoidal state.

The carbazole moiety in **4a** is planar and allows for the effect of planarisation and increased conjugation of the phenyl rings to be accounted for. As the emission in **5a** is more red-shifted than **4a**, it is inferred that the dihedral angle plays a more dominant role in red-shifting the emission than does planarisation of the phenyl rings. It also raises the question of how planarity is defined. For example, if the phenyl rings become coplanar but θ_1 increases to 90°, is the molecule more, or less planar? This should be carefully considered when assigning overall molecular conformation as more or less planar. The larger ground-state θ_1 values in **4a** and **5a** mean that a smaller change in magnitude is required to increase the dihedral angle to the nominal TICT-state angle of 90° after application of force compared to **3a**, potentially explaining why they have smaller MFC red-shifts. Further, the higher energy emission maxima of **3a**-G (529 nm) and **4a**-G (524 nm) relative to **5a**-C (540 nm) indicate that these PBs are not reaching a 90° dihedral angle in the excited state. Thus, the degree of the increase in dihedral angle on relaxation is not strictly defined. What can be defined is the trend of the greater the dihedral angle (which is correlated with an increase in C_P–N_1), the more red-shifted the emission. It is important to note here that ground-state planarisation and excited-state twisting are not mutually exclusive (and *vice versa*). For example, if there is release of strain energy after force application due to perturbation of intermolecular interactions, the ground-state conformation may become more planar.[41] But now that the rigidifying intermolecular interactions are perturbed, an excited molecule may undergo a greater increase in dihedral angle than it could pre-application of force, if the TICT-like state is the lowest energy excited-state conformation. In this hypothetical situation, the absorption could be red-shifted due to increased planarisation, but the emission red-shifted due to decreased planarisation. This is raised to reinforce the point that the ground and excited states should not be conflated and must be treated separately.

Comparison of 1a with 3a. The two PBs crystallise remarkably with near identical packing. This serendipity allows for a direct structure–property comparison. Crystal structure data for **1a** and **3a** reveal that they have near identical packing, space group and unit cell parameters. Crystal packing similarity was determined using the COMPACK method.[42] A packing overlay based on 15 molecule clusters calculated a low root-mean-square deviation value of 0.399 Å with 14 molecules in common, representing strong similarity (Fig. 5a). This method is useful as it is not dependent on space group or unit cell. The nature of the intermolecular interactions can be quantified using the CrystalExplorer software package and represented by total energy frameworks. These are given in Fig. S13† and confirm that the intermolecular interactions found in **1a** are retained in **3a**.

Having confirmed the strong similarity in packing and interaction types/energies, the emission spectra of **1a**-C and **3a**-C may be compared and correlated with structural differences. The emission band of **3a**-C is narrower than that of **1a**-C and encompassed by the broad emission range of **1a**-C, with both having very similar maxima (Fig. 5b; **1a**-C – 469 nm, **3a**-C – 462 nm). An overlay of both structures looking down C_P–N_1 on the *N*,*N*-diphenylamino end highlights the key structural difference (zoomed region in Fig. 5a). The phenyl ring adjacent to the methyl group is displaced giving **3a** a larger θ_1 and C_P–N_1 is elongated (**1a** – 1.351 Å, **3a** – 1.366 Å). This indicates that there is less conformational freedom in **3a**, due to the steric restraints imposed by the methyl group. For example, the lack of higher energy shoulder emission band is consistent with **3a** being unable to adopt the same geometry as **1a** with respect to the displaced phenyl ring. To illustrate that **3a** has overall more red-shifted emission than **1a**, the annealed forms provide a useful comparison. These represent the most blue-shifted emission maxima for all PBs, likely due to a higher degree of crystallinity. The emission maxima of these forms indicate a more obvious red-shift in **3a** compared to **1a** (Fig. 5c; **1a**-An – 439 nm, **3a**-An – 459 nm). As will be discussed in the next section, the PXRD indicates no phase change, thus it is fair to say that they both retain the same crystalline phase and that **3a** has a more red-shifted emission than **1a** in crystalline form. The spectral difference is also evident in the mechanically ground forms where the emission maximum in **3a** is significantly more red-shifted than **1a** (**1a**-G – 502 nm, **3a**-G – 529 nm). However, this analysis neglects subtle changes in PXRD patterns that may indicate structural differences and will be returned to in the electron diffraction section.

Several reports have postulated that excited-state twisting can occur in crystalline materials if there is enough space to accommodate the geometry change.[43] The similarity between **1a** and **3a** suggests that there is conformational freedom in **1a** without disrupting the crystallinity. This access to more conformations can explain the broader emission in **1a**-C. Thus, this packing formation can facilitate a certain degree of conformational freedom, and this can be directly correlated to changes in fluorescence. The more red-shifted emission maximum of **3a**-G compared to **1a**-G (Δ27 nm) can be rationalised by **3a**-G having access to greater θ_1 values than **1a**-G, although, as mentioned earlier, this is still less than 90° for both compounds. In aggregated forms, there will generally be restriction of motion, the degree of which will depend on parameters such as the packing density and the nature of the intermolecular interactions. Thus, as **3a**-C has a larger θ_1 than

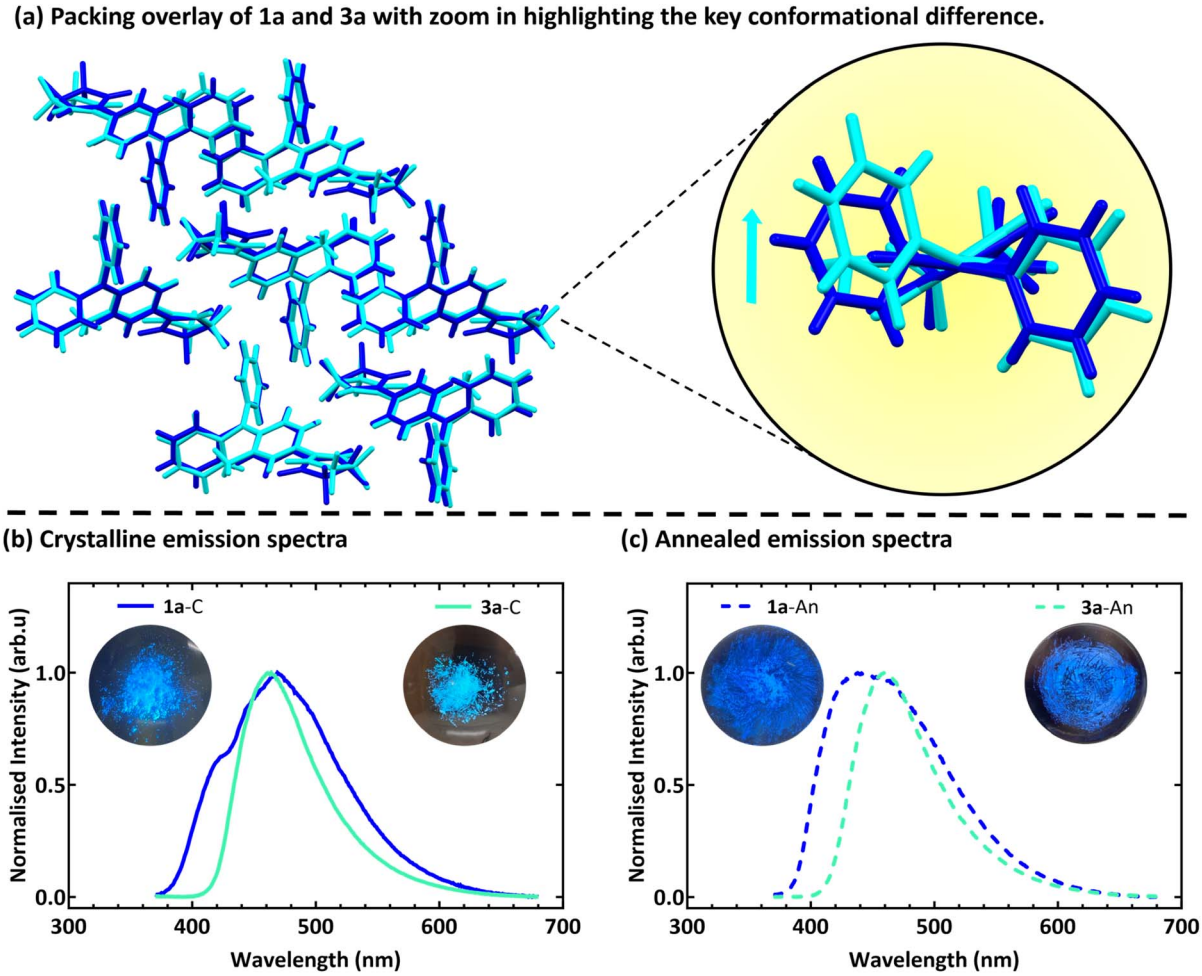

Fig. 5 (a) Crystal packing diagram overlay of **1a** (blue) and **3a** (cyan) looking down the *b*-axis and showing several molecules with strong packing similarity. A zoomed in region of one overlaid pair highlights the key conformational difference. Viewing down the C_P–N_1 bond on the *N*,*N*-diphenyl side of the molecules shows that the methyl group pushes a phenyl ring out of the plane relative to **1a**; (b) normalised solid-state fluorescence spectra in crystalline forms showing the narrower band of **3a** with an energy distribution encompassed within that of **1a**. The excitation wavelength is 350 nm for both. Inset: images of **1a**-C (left) and **3a**-C (right) under 365 nm UV irradiation; (c) normalised solid-state fluorescence spectra in annealed forms showing the narrower band of **3a** with a red-shifted maximum compared to **1a**. The excitation wavelength is 350 nm for both. Inset: images of **1a**-An (left) and **3a**-An (right) under 365 nm UV irradiation. Emission spectra and images of **1a** are reproduced from previously published research with permission and are copyright RSC (*J. Mat. C*).[3]

1a-C, it is posited that after force application **3a**-G will still reach larger θ_1 values than **1a**-G.

Another important aspect to consider is the local polarity experienced by a molecule in a crystal due to the surrounding intermolecular interactions. The interactions often change on application of force in the amorphous regions, which can effectively result in changes to the local polarity.[2] This can then lead to spectral shifts, much like solvatofluorochromism.[44] While this may play a role, the evidence presented suggests it is not a dominant cause of the spectral shifts.

Overall, it is highly unlikely that the red-shifts observed in the mechanically ground forms are the result of planarisation about the C_P–N_1 bond due to the steric hindrance provided by the methyl groups or carbazole hydrogens blocking this process. For example, this is clear in **5a**, where the two methyl groups inhibit a decrease in θ_1. Further, if we discount any methyl group electronic effect or local polarity effects, then elongation of C_P–N_1 and increased θ_1 are the key differences that lead to a red-shifted emission. Planarisation about the C_E–N_2 bond can also be ruled out from the methyl group at the two-position in **2a**, which also shows a red MFC shift comparable to **1a**.

Powder X-ray diffraction. Powder patterns were collected at room temperature for the new compounds in crystalline powder forms and compared with simulated patterns from SC-XRD data (Fig. S14–S20†). For the PBs, additional data was collected in the four forms under study (Fig. S18–S20†). Qualitatively, **3a** and **5a** show broadened peaks with weakened intensities after application of force, indicating a mixture of crystalline and amorphous phases. No new phase was detected in either. Contrastingly, **4a** transitioned completely to an amorphous phase in the G form, indicative of overall weaker intermolecular interactions. The increased intensities and sharper peaks in the R and An forms indicate restoration of crystallinity for all PBs.

The partial retention of crystallinity in **3a** prompted us to probe any subtle structural changes in more detail.

Electron diffraction on 3a. To further investigate the G form of **3a**, electron diffraction was performed on several microcrystalline grains at 100 K and 294 K (Tables S14–S16† for data parameters and processing statistics). The grains chosen were less than 2 μm in diameter and provided diffraction images at resolution less than 1 Å (Fig. S21 and S22†). This powerful technique allows for full structure determination on the red-shifted G form particles to probe whether any changes have occurred that can explain the change in emission colour. This is important as subtle changes in PXRD patterns are often difficult to analyse due to several complicating variables, including peak overlap concealing individual peak intensities.[45] Thus, it should not be assumed that because the PXRD pattern does not show an obvious phase change, that there is not an important, albeit likely minor, structural change occurring. In this case, the room temperature ED and SC-XRD overlay shows that the structure is essentially the same (Fig. 6). This is the same result we noted previously for **1a**, providing further strong evidence for the existence of an amorphous coating on microcrystalline material. This data allows us to be confident that the PXRD of the G form is indeed showing partial retention of the same long-range order (*i.e.* same crystal phase) along with an increased amorphous contribution. But, as mentioned, due to the complications inherent in PXRD pattern analysis, this is not necessarily the case, and thus ED provides valuable information to verify that the conclusion drawn of no additional crystalline phase being present is valid.

Quantum chemical calculations

Having experimentally ascertained CT states to be involved in the radiative transitions, and θ_1 as the parameter likely to be most influential on the emission profile, quantum chemical calculations were undertaken to determine the validity of this hypothesis. Coordinates for the three new PBs, as well as **1a**, were acquired from the room temperature crystal structure data and linear-response time-dependent density functional theory[46] (TD-DFT) calculations were carried out to obtain vertical excitation energies and natural transition orbitals[47] (NTOs). The latter allow better analysis of relevant donor and acceptor orbitals during an electronic excitation compared to a more conventional molecular orbital analysis. To properly describe CT transitions, the ωB97XD3 [48] method and the Ahlrichs-type split-valence triple-ζ atomic-orbital basis set with one set of polarisation functions def2-TZVP[49] were chosen, and calculations were carried out with ORCA 5.0.4.[50] The crystal coordinates were chosen to simulate the transitions in the relatively fixed geometries present in the crystal and thus no geometry optimisations were performed. This assumes isolated molecules in the gas phase with no intermolecular short-range or long-range electronic effects and simulates the expected orbitals and vertical transition energies. The first singlet excited state transition in **1a** is very similar to that of **3a**, consisting of mixed character with contributions from enolate, pyridinium, and the *N*,*N*-diphenylamino moieties (Fig. 7a and b). The donor NTO is predominantly composed of enolate, pyridinium π-orbital, and *N*,*N*-diphenylamino nitrogen non-bonding orbital contribution. The acceptor NTO is more distributed across the molecule with π* character at the pyridinium moiety. **4a** also shows this mixed enolate and pyridinium π-orbital character but with a greater contribution in the donor orbital from the phenyl rings in the carbazole moiety (Fig. 7c). In **5a**, the contribution from the phenyl rings is qualitatively even greater than in **4a** (Fig. 7d). This indicates a mixed LE/CT or CT/CT transition involving both enolate and *N*,*N*-diphenylamino moieties as electron donors. Calculated first singlet excited-state vertical transition energies (λ) red-shift from **1a** (309.1 nm) to **3a** (314.1 nm) to **4a** (342.5 nm) to **5a** (352.5 nm), in accordance with the experimental data in the C forms for **3a**, **4a**, and **5a**. For **1a**, the vertical transition energy is blue-shifted by 5 nm relative to **3a**, and this aligns with the An form of **1a** having a blue-shifted emission maximum (see Comparison of **1a** with **3a** section and Fig. 5). All values are systematically blue-shifted due to the ωB97XD3 method chosen.[48] Additional calculations were performed with CAM-B3LYP[11] to verify these trends and are given in the ESI (Fig. S23).† Together, these support the experimental evidence showing that increasing θ_1 leads to a greater orbital contribution from the *N*,*N*-diphenylamino moiety and red-shifts the emission, and not planarisation. Furthermore, the presence of conformationally less restricted molecules in the amorphous phase of the mechanically ground forms can result in greater excited-state twisting and the observed MFC red-shifts.

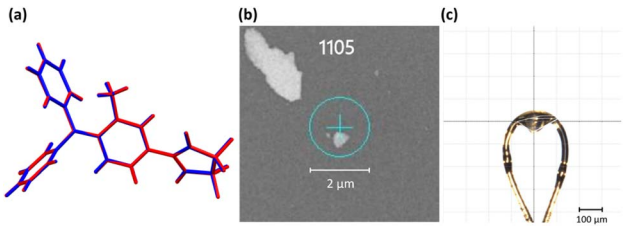

Fig. 6 (a) Electron diffraction and SC-XRD structure overlay for **3a** – ED (red) and SC-XRD (blue); (b) visual image of representative grain used for ED data collection; (c) visual image of crystal used for SC-XRD. Note the scale bars.

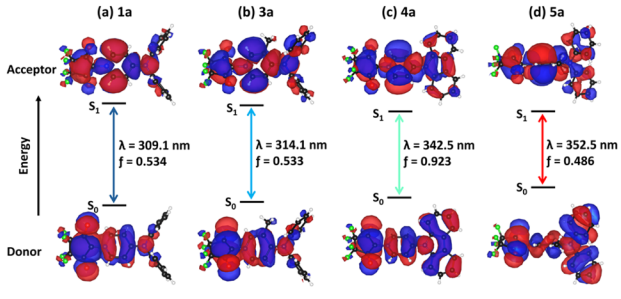

Fig. 7 Natural transition orbitals, vertical transition energies (λ), and oscillator strengths (f) calculated in the gas phase for the $S_0 \rightarrow S_1$ transition in (a) **1a**; (b) **3a**; (c) **4a**; and (d) **5a**. Calculations were performed at the ωB97xD3 def2-TZVP level, on crystal coordinates. Isosurface values are 0.01.

Conclusions

A thorough mechanistic understanding of MFC materials is beneficial for establishing design principles to prepare new MFC materials so they can be used effectively in cutting-edge applications. By introducing judiciously placed methyl groups or rigidification of phenyl rings, a steric induced increase in dihedral angle between excited-state donor and acceptor moieties allows one to probe the nature of the geometry changes in MFC compounds. In this study of PBs, an increase in dihedral angle between *N*,*N*-diphenylamino and pyridinium results in red-shifts of emission. Application of mechanical force induces perturbation of intermolecular interactions and enables access to more twisted excited states in an amorphous phase. This is supported by PXRD and ED experiments, which show that crystalline and amorphous phases can coexist. Two of the compounds differing by only one methyl group crystallise in the same space group with near identical packing, but different emission properties, serendipitously allowing for a direct comparison of structure and emission. Regarding **3a**, the increased dihedral angle and *N*,*N*-diphenylamino-pyridinium bond length, as well as reduced conformational freedom between donor and acceptor induced by the methyl group are responsible for the red-shifted and sharper emission profile. Planarisation of the *N*,*N*-diphenylamino donor moiety is found to be less influential in red-shifting the emission than the dihedral angle between this donor and acceptor. This is shown by comparing a planar carbazole donor analogue (**4a**) to a *N*,*N*-diphenylamine analogue that is twisted by two methyl groups (**5a**).

Using this methodology to adjust the dihedral angle, the nature of the geometry change may potentially be solved for other MFC systems, whether twisting, planarisation, or neither. It is also an effective approach for tuning the emission wavelength and the singlet-triplet energy gap, which is one of the properties required for effective TADF.

More generally, one must be careful when assigning a red-shift in emission on application of mechanical force to planarisation, as many donor–acceptor systems have been shown to exhibit excited-state twisting. Thus, a more planar conformation does not necessitate red-shifted spectra. Therefore, employing methyl groups and rigidification judiciously can be a straightforward strategy for elucidating the MFC mechanism, as well as tuning the optical properties of donor–acceptor type systems. This leads to a deeper understanding of the optical properties of stimuli-responsive solid-state materials.

Data availability

The data underpinning this study are included in the published article and as part of the ESI,† or available from the authors on request.

Author contributions

All authors have contributed significantly to the paper, each contributing to the writing, review and editing of the paper. P. W. M. and C. R. conceptualisation, data curation, formal analysis, investigation, methodology, writing – review and editing. P. W. M. investigation, writing – original draft. L. G. data curation, writing – review and editing, formal analysis, methodology. C. R. and L. G. funding acquisition, resources. All authors agree with the content of the manuscript.

Conflicts of interest

There are no conflicts to declare.

Acknowledgements

The authors gratefully acknowledge Prof. Kellie Tuck and Assoc. Prof. Toby Bell from Monash University for access to spectroscopic equipment and support. Dr Pierre Le Magueres and Dr Lee M. Daniels from Rigaku Americas Corporation for acquisition and analysis of electron diffraction data. The Monash Chemistry team (Dr Alasdair McKay, Kai Robinson, Dr Boujemaa Moubaraki and Dr Craig Forsyth). P. W. M. thanks Monash University and the Australian Government for a Research Training Program Scholarship. The authors acknowledge the use of facilities within the Monash X-ray Platform, as well as Dr Dale R. Lonsdale for preliminary calculations on some of these systems. L. G. is grateful for generous allocations of computational resources from the National Computational Infrastructure (NCI) Facility within the National Computational Merit Allocation Scheme (project fk5), and Research Platform Services (ResPlat) at The University of Melbourne (project punim0094). This research was additionally supported by the Research Computing Services NCI access scheme at The University of Melbourne. L. G. and C. R. thank the ARC for funding this research (DP230102664).

Notes and references

1 (*a*) S. Ito, *J. Photochem. Photobiol., C*, 2022, **51**, 100481; (*b*) J. Xu and Z. Chi, in *Mechanochromic Fluorescent Materials: Phenomena, Materials and Applications*, ed. J. Xu and Z. Chi, The Royal Society of Chemistry, 2014, ch. 1, pp. 1; (*c*) Z. Chi, X. Zhang, B. Xu, X. Zhou, C. Ma, Y. Zhang, S. Liu and J. Xu, *Chem. Soc. Rev.*, 2012, **41**, 3878.
2 Y. Sun, Z. Lei and H. Ma, *J. Mater. Chem. C*, 2022, **10**, 14834.
3 J. Zhao, Z. Chi, Y. Zhang, Z. Mao, Z. Yang, E. Ubba and Z. Chi, *J. Mater. Chem. C*, 2018, **6**, 6327.
4 C. Wang, W. Chi, Q. Qiao, D. Tan, Z. Xu and X. Liu, *Chem. Soc. Rev.*, 2021, **50**, 12656.
5 Z. R. Grabowski, K. Rotkiewicz and A. Siemiarczuk, *J. Lumin.*, 1979, **18–19**, 420.
6 G. Haberhauer, R. Gleiter and C. Burkhart, *Chem.–Eur. J.*, 2016, **22**, 971.
7 (*a*) K. A. Zachariasse, M. Grobys, T. von der Haar, A. Hebecker, Y. V. Il'ichev, Y. B. Jiang, O. Morawski and W. Kühnle, *J. Photochem. Photobiol., A*, 1996, **102**, 59; (*b*) T. von Der Haar, A. Hebecker, Y. Il'Ichev, Y.-B. Jiang, W. Kühnle and K. A. Zachariasse, *Recl. Trav. Chim. Pays-*

Bas, 1995, **114**, 430; (*c*) T. Yoshihara, S. I. Druzhinin and K. A. Zachariasse, *J. Am. Chem. Soc.*, 2004, **126**, 8535.
8 Z. R. Grabowski, K. Rotkiewicz and W. Rettig, *Chem. Rev.*, 2003, **103**, 3899.
9 Y. Che and D. F. Perepichka, *Angew. Chem., Int. Ed.*, 2021, **60**, 1364.
10 (*a*) C. Zhong, *Phys. Chem. Chem. Phys.*, 2015, **17**, 9248; (*b*) C. A. Guido, B. Mennucci, D. Jacquemin and C. Adamo, *Phys. Chem. Chem. Phys.*, 2010, **12**, 8016.
11 T. Yanai, D. P. Tew and N. C. Handy, *Chem. Phys. Lett.*, 2004, **393**, 51.
12 (*a*) A. Datar, S. Gudivada and D. A. Matthews, *J. Phys. Chem. A*, 2023, **127**, 4643; (*b*) C. Gajo, D. Shchepanovska, J. F. Jones, G. Karras, P. Malakar, G. M. Greetham, O. A. Hawkins, C. J. C. Jordan, B. F. E. Curchod and T. A. A. Oliver, *J. Phys. Chem. B*, 2024, **128**, 11768.
13 M. Segado, I. Gómez and M. Reguero, *Phys. Chem. Chem. Phys.*, 2016, **18**, 6861.
14 (*a*) Y. Wang, D. Xu, H. Gao, Y. Wang, X. Liu, A. Han, C. Zhang and L. Zang, *J. Phys. Chem. C*, 2018, **122**, 2297; (*b*) Q. Qi, J. Zhang, B. Xu, B. Li, S. X.-A. Zhang and W. Tian, *J. Phys. Chem. C*, 2013, **117**, 24997; (*c*) B. Xu, Q. Qi, J. Zhang and W. Tian, in *Mechanochromic Fluorescent Materials: Phenomena, Materials and Applications*, Royal Society of Chemistry, 2014, pp. 236.
15 (*a*) D. Sun, Y. Wu, X. Han and S. Liu, *Nat. Commun.*, 2023, **14**, 4190; (*b*) J. Wei, B. Liang, X. Cheng, Z. Zhang, H. Zhang and Y. Wang, *RSC Adv.*, 2015, **5**, 71903; (*c*) Y. Zhang, J. Sun, G. Zhuang, M. Ouyang, Z. Yu, F. Cao, G. Pan, P. Tang, C. Zhang and Y. Ma, *J. Mater. Chem. C*, 2014, **2**, 195; (*d*) Y. Zhang, J. Sun, G. Bian, Y. Chen, M. Ouyang, B. Hu and C. Zhang, *Photochem. Photobiol. Sci.*, 2012, **11**, 1414; (*e*) H. Liu, H. Zhu, B. Liu, J. Bai, J. Peng, H. Zhang and J. Jia, *J. Lumin.*, 2025, **279**, 121034; (*f*) S. Fu, Y. Tan, S. Zhang, J. Lv, X. Feng, D. Xu and X. Liu, *Dyes Pigm.*, 2022, **198**, 109983.
16 (*a*) P. S. Hariharan, N. S. Venkataramanan, D. Moon and S. P. Anthony, *J. Phys. Chem. C*, 2015, **119**, 9460; (*b*) P. Shi, D. Deng, C. He, L. Ji, Y. Duan, T. Han, B. Suo and W. Zou, *Dyes Pigm.*, 2020, **173**, 107884; (*c*) W. Luo, Y. Tang, X. Zhang, Z. Wu and G. Wang, *Adv. Opt. Mater.*, 2023, **11**, 2202259.
17 K. Mizuguchi, H. Kageyama and H. Nakano, *Mater. Lett.*, 2011, **65**, 2658.
18 W. Chi, Q. Qiao, R. Lee, W. Liu, Y. S. Teo, D. Gu, M. J. Lang, Y. T. Chang, Z. Xu and X. Liu, *Angew. Chem., Int. Ed.*, 2019, **58**, 7073.
19 (*a*) J. Chen, S. Tan, Y. Yu, S. Zhang, W. Li, Q. Song, Y. Dong, C. Zhang and W.-Y. Wong, *J. Lumin.*, 2021, **237**, 118179; (*b*) Z. Xie, T. Yu, J. Chen, E. Ubba, L. Wang, Z. Mao, T. Su, Y. Zhang, M. P. Aldred and Z. Chi, *Chem. Sci.*, 2018, **9**, 5787; (*c*) J. M. Lee, S. B. Yuk, J. W. Namgoong and J. P. Kim, *Dyes Pigm.*, 2021, **185**, 108864.
20 S. I. Druzhinin, V. A. Galievsky, A. Demeter, S. A. Kovalenko, T. Senyushkina, S. R. Dubbaka, P. Knochel, P. Mayer, C. Grosse, D. Stalke and K. A. Zachariasse, *J. Phys. Chem. A*, 2015, **119**, 11820.
21 (*a*) S. I. Druzhinin, S. A. Kovalenko, T. Senyushkina and K. A. Zachariasse, *J. Phys. Chem. A*, 2007, **111**, 12878; (*b*) S. I. Druzhinin, S. R. Dubbaka, P. Knochel, S. A. Kovalenko, P. Mayer, T. Senyushkina and K. A. Zachariasse, *J. Phys. Chem. A*, 2008, **112**, 2749; (*c*) S. I. Druzhinin, S. A. Kovalenko, T. A. Senyushkina, A. Demeter, R. Machinek, M. Noltemeyer and K. A. Zachariasse, *J. Phys. Chem. A*, 2008, 112–8238; (*d*) K. A. Zachariasse, T. v. d. Haar, A. Hebecker, U. Leinhos and W. Kuhnle, *Pure Appl. Chem.*, 1993, 65–1745; (*e*) W. Rettig and B. Zietz, *Chem. Phys. Lett.*, 2000, **317**, 187; (*f*) J. Liu, Y. Feng, H.-J. Yin, T. He, K.-Z. Wang, G. Long and C.-J. Yao, *J. Phys. Chem. C*, 2023, 127–5567; (*g*) J. S. Ward, R. S. Nobuyasu, A. S. Batsanov, P. Data, A. P. Monkman, F. B. Dias and M. R. Bryce, *Chem. Commun.*, 2016, **52**, 2612.
22 C. Chen, R. Huang, A. S. Batsanov, P. Pander, Y.-T. Hsu, Z. Chi, F. B. Dias and M. R. Bryce, *Angew. Chem., Int. Ed.*, 2018, **57**, 16407.
23 P. W. McDonald and C. Ritchie, *Chem. Commun.*, 2024, **60**, 3051.
24 J. Xu, B. Zhang, M. Jansen, L. Goerigk, W. W. H. Wong and C. Ritchie, *Angew. Chem., Int. Ed.*, 2017, **56**, 13882.
25 J. Gamboa Varela, A. De Chatterjee, P. Guevara, V. Ramirez, A. J. Metta-Magaña, D. Villagrán, A. Varela-Ramirez, S. Das and J. E. Nuñez, *J. Biol. Inorg. Chem.*, 2014, **19**, 967.
26 Y. Chen, X. Li, W. Che, L. Tu, Y. Xie and Z. Li, *J. Mater. Chem. C*, 2021, **9**, 11738.
27 (*a*) W. Rettig and R. Gleiter, *J. Phys. Chem.*, 1985, **89**, 4676; (*b*) Z. Zhang, C.-L. Chen, Y.-A. Chen, Y.-C. Wei, J. Su, H. Tian and P.-T. Chou, *Angew. Chem., Int. Ed.*, 2018, **57**, 9880.
28 (*a*) R. W. Newberry and R. T. Raines, *Acc. Chem. Res.*, 2017, **50**, 1838; (*b*) H. B. Burgi, J. D. Dunitz and E. Shefter, *J. Am. Chem. Soc.*, 1973, **95**, 5065.
29 M. Suzuki, M. Fujita, T. Takemura and H. Baba, *Bull. Chem. Soc. Jpn.*, 1988, **61**, 3461.
30 P. W. McDonald, J. Xu, D. R. Lonsdale, I. Jones, B. Poggi, R. P. Cox, S. Aloise, A. D. Scully, C. Allain, L. Bodelot, S. A. Moggach, T. D. M. Bell, R. Métivier, S. G. B. Furness, L. Goerigk and C. Ritchie, *J. Mater. Chem. C*, 2024, **12**, 19371.
31 E. Taipale, N. A. Durandin, J. K. Salunke, N. R. Candeias, T.-P. Ruoko, J. S. Ward, A. Priimagi and K. Rissanen, *Mater. Adv.*, 2022, **3**, 1703.
32 R. Englman and J. Jortner, *Mol. Phys.*, 1970, **18**, 145.
33 J. M. Dos Santos, C.-Y. Chan, S. Tang, D. Hall, T. Matulaitis, D. B. Cordes, A. M. Z. Slawin, Y. Tsuchiya, L. Edman, C. Adachi, Y. Olivier and E. Zysman-Colman, *J. Mater. Chem. C*, 2023, **11**, 8263.
34 X. Qian, F. Chu, W. Zhou, Z. Zheng, X. Chen and Y. Zhao, *J. Phys. Chem. Lett.*, 2023, 3335.
35 L. S. Cui, H. Nomura, Y. Geng, J. U. Kim, H. Nakanotani and C. Adachi, *Angew. Chem., Int. Ed.*, 2017, **56**, 1571.
36 (*a*) X. Xu and B. Yan, *Phys. Chem. Chem. Phys.*, 2023, **25**, 1457; (*b*) Y. Liu, C. Li, Z. Ren, S. Yan and M. R. Bryce, *Nat. Rev. Mater.*, 2018, **3**, 18020; (*c*) M. He, C. Ding, H. Guo and Q. Li, *Responsive Mater.*, 2024, **2**, e20240014; (*d*) J.-M. Teng, Y.-F. Wang and C.-F. Chen, *J. Mater. Chem. C*, 2020, **8**, 11340.

37 (*a*) M. Nespolo and A. H. Benahsene, *J. Appl. Crystallogr.*, 2021, **54**, 1594; (*b*) E. Taipale, M. Siepmann, K. N. Truong and K. Rissanen, *Chem.–Eur. J.*, 2021, **27**, 17412.
38 P. Metrangolo, J. S. Murray, T. Pilati, P. Politzer, G. Resnati and G. Terraneo, *Cryst. Growth Des.*, 2011, **11**, 4238.
39 Z.-Q. Li, J.-H. Tang, Y.-Q. He, Z.-L. Gong, J.-Y. Shao and Y.-W. Zhong, *Cryst. Growth Des.*, 2021, **21**, 1854.
40 (*a*) M. Morita, S. Yamada and T. Konno, *New J. Chem.*, 2020, **44**, 6704; (*b*) S. Yamada and T. Konno, *Chem. Rec.*, 2023, **23**, e202300094; (*c*) K. Kobayashi, S. Yamada, M. Morita, T. Sakurai, M. Yasui and T. Konno, *J. Mater. Chem. C*, 2025, **13**, 1369.
41 (*a*) B. Xu, Z. Chi, J. Zhang, X. Zhang, H. Li, X. Li, S. Liu, Y. Zhang and J. Xu, *Chem.–Asian J.*, 2011, **6**, 1470; (*b*) C. Wang and Z. Li, *Mater. Chem. Front.*, 2017, **1**, 2174.
42 J. A. Chisholm and S. Motherwell, *J. Appl. Crystallogr.*, 2005, **38**, 228.
43 (*a*) H. Naito, K. Nishino, Y. Morisaki, K. Tanaka and Y. Chujo, *Angew. Chem., Int. Ed.*, 2017, **56**, 254; (*b*) J. Li, C. Yang, X. Peng, Y. Chen, Q. Qi, X. Luo, W.-Y. Lai and W. Huang, *J. Mater. Chem. C*, 2018, **6**, 19.
44 C. Reichardt, *Chem. Rev.*, 1994, **94**, 2319.
45 (*a*) K. D. M. Harris, M. Tremayne and B. M. Kariuki, *Angew. Chem., Int. Ed.*, 2001, **40**, 1626; (*b*) S. Racioppi, A. Otero-de-la-Roza, S. Hajinazar and E. Zurek, *Digital Discovery*, 2025, **4**, 73.
46 (*a*) E. Runge and E. K. U. Gross, *Phys. Rev. Lett.*, 1984, **52**, 997; (*b*) R. Bauernschmitt and R. Ahlrichs, *Chem. Phys. Lett.*, 1996, **256**, 454.
47 R. L. Martin, *J. Chem. Phys.*, 2003, **118**, 4775.
48 Y.-S. Lin, G.-D. Li, S.-P. Mao and J.-D. Chai, *J. Chem. Theory Comput.*, 2013, **9**, 263.
49 F. Weigend and R. Ahlrichs, *Phys. Chem. Chem. Phys.*, 2005, **7**, 3297.
50 (*a*) F. Neese, *Wiley Interdiscip. Rev.:Comput. Mol. Sci.*, 2012, **2**, 73; (*b*) F. Neese, *Wiley Interdiscip. Rev.:Comput. Mol. Sci.*, 2022, **12**, e1606.